Cell Reports
Physical Science

CellPress
OPEN ACCESS

Article

# Tuning counterion chemistry to reduce carrier localization in doped semiconducting carbon nanotube networks

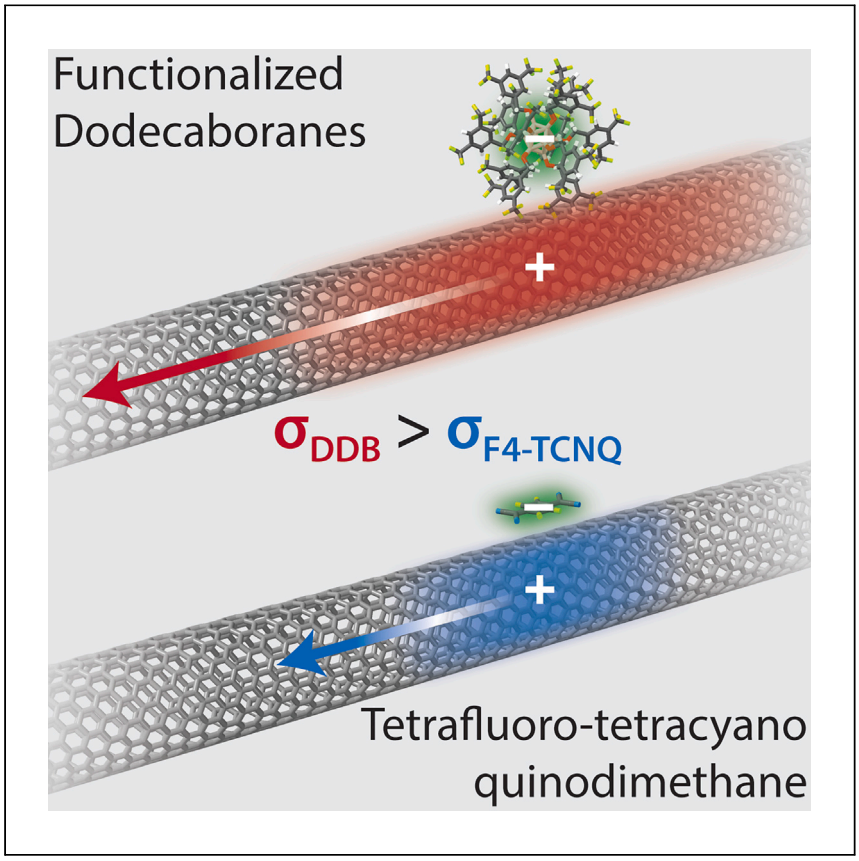


Murrey et al. demonstrate improved transport of chemically injected charge carriers in enriched semiconducting carbon nanotube networks. By employing functionalized icosahedral dodecaborane clusters as the dopant, the coulombic interactions between the hole and the associated counteranion can be reduced. This enables enhanced thermoelectric transport and power factor.

Tucker L. Murrey, Taylor J. Aubry, Omar Leon Ruiz, ..., Tobias Hertel, Jeffrey L. Blackburn, Andrew J. Ferguson

jeffrey.blackburn@nrel.gov (J.L.B.)
andrew.ferguson@nrel.gov (A.J.F.)

## Highlights

Molecular charge-transfer dopant with electron affinity tunable by chemical structure

Carrier-counterion interactions reduced by localization of extracted electron

Delocalization of hole improves thermoelectric charge transport

Thermoelectric power factor surpasses best for enriched carbon nanotube networks

Murrey et al., Cell Reports Physical Science 4, 101407
May 17, 2023 
https://doi.org/10.1016/j.xcrp.2023.101407

Cell Reports
Physical Science

CellPress
OPEN ACCESS

Article

# Tuning counterion chemistry to reduce carrier localization in doped semiconducting carbon nanotube networks

Tucker L. Murrey,[1,2] Taylor J. Aubry,[2] Omar Leon Ruiz,[3] Kira A. Thurman,[2] Klaus H. Eckstein,[4] Evan A. Doud,[3] Julia M. Stauber,[3] Alexander M. Spokoyny,[3] Benjamin J. Schwartz,[3] Tobias Hertel,[4] Jeffrey L. Blackburn,[2,*] and Andrew J. Ferguson[2,5,*]

## SUMMARY

**Understanding and controlling the impact that electrostatic interactions have on the transport of injected charge carriers is important for the utilization of pi-conjugated semiconductors in opto-electronic applications. Here, we explore the impact of dopant chemical and electronic structure on the doping efficacy and charge carrier transport in semiconducting single-walled carbon nanotube (s-SWCNT) networks using molecular charge-transfer dopants based on functionalized icosahedral dodecaborane (DDB) clusters. Calculations indicate that localization of electron density on the DDB core reduces the coulombic interactions that contribute to hole localization in the s-SWCNTs, thereby improving charge carrier transport. The enhanced delocalization produces an increase in the electrical conductivity and thermopower at lower charge carrier densities, yielding enhanced thermoelectric transport and a thermoelectric power factor that surpasses the previous best in class for enriched s-SWCNT thin-film networks. This strategy can be applied broadly across pi-conjugated semiconductors to tune and enhance performance in a variety of energy harvesting devices.**

## INTRODUCTION

Semiconducting single-walled carbon nanotubes (s-SWCNTs) and related organic semiconducting (e.g., polymer) systems exhibit chemical and physical properties that mark them as a promising platform for a variety of optoelectronic and energy harvesting technologies.[1–4] However, realization of their significant potential will require careful control of the charge carrier density and an understanding of the subsequent charge carrier transport in conductive thin films.[5] Molecular charge-transfer dopants offer an effective means to fine-tune the carrier density in organic carbon-based semiconducting systems,[6,7] including carbon nanotubes.[3,8–10]

A long-standing fundamental question regarding molecular doping of low-dielectric organic semiconductors is the degree to which a charge injected by a redox molecule can escape the coulomb potential of the associated molecular counterion.[6,7,11,12] Furthermore, rational strategies to reduce this coulomb attraction and concomitant charge carrier localization could lead to enhanced performance in many envisioned applications for semiconducting polymers and SWCNTs, such as thin-film and bulk heterojunction solar cells,[13–15] transparent conducting thin films for solar cells[16] and other electronic devices, and thermoelectric (TE) energy harvesting devices.[3,4]

[1]Department of Material Science and Engineering, University of California, Davis, Davis, CA 95616, USA

[2]Materials, Chemical and Computational Science Directorate, National Renewable Energy Laboratory (NREL), Golden, CO 80401, USA

[3]Department of Chemistry and Biochemistry, University of California, Los Angeles, Los Angeles, CA 90095-1569, USA

[4]Institute of Physical and Theoretical Chemistry, Julius-Maximilians-Universität Würzburg, Würzburg, Germany

[5]Lead contact

*Correspondence: jeffrey.blackburn@nrel.gov (J.L.B.), andrew.ferguson@nrel.gov (A.J.F.)

https://doi.org/10.1016/j.xcrp.2023.101407

Detailed transport measurements that simultaneously track the electrical conductivity (σ) and thermopower (α) as a function of doping density have emerged as a promising platform for understanding charge carrier transport and (de)localization in doped organic semiconductors.[17,18] The power of this approach lies in the unique and intertwined dependences of these two fundamental properties on charge carrier density and mobility.[17] Recently, carrier localization effects were explicitly considered in the so-called semilocalized transport (SLoT) model,[18] which demonstrated that coulombic potential wells limit charge carrier transport in both conjugated polymers and s-SWCNT networks. In other words, localization-limited transport arises from coulombic interactions between the hole density injected into the s-SWCNTs and the oppositely charged proximal dopant counterions.[19] Despite these observations, there have not been any systematic studies aimed at controlling carrier-counterion interactions in nanocarbon materials to enhance carrier delocalization or at improving charge carrier transport.

In contrast, several approaches have been explored to manipulate the interactions between dopant counterions and the carrier density injected into conjugated polymers. Yamashita et al. demonstrated enhanced doping efficiency and charge transport in poly[2,5-bis(3-tetradecylthiophen-2-yl)thieno[3,2-*b*]thiophene] (PBTTT-C14) via an electrolyte-mediated anion exchange process.[20] Recent studies of the ion exchange process have further increased doping efficiency and correlated the presence of larger anions to more delocalized hole polarons in polymers.[21–23] Recently, a class of molecular oxidants based on functionalized dodecaborane (DDB) clusters have been introduced for effective p-type doping of conjugated polymers. These DDB-based dopants possess tunable redox properties,[24,25] and their large molecular size results in a weakly coordinating anion in the reduced state,[26] characteristics that yield enhanced hole transport in poly[3-hexylthiophene-2,5-diyl] (P3HT) films compared with samples doped by the well-studied p-type dopant 2,3,5,6-tetrafluoro-7,7,8,8-tetracyanoquinodimethane ($F_4$TCNQ).[25,27]

Here, we employ several DDB dopants perfunctionalized with ether-linked fluorinated benzyl moieties[26] to perform the first systematic study of the influence of dopant counterion chemistry on charge carrier transport and (de)localization in networks of enriched s-SWCNTs. Enriched s-SWCNT networks hold several key advantages including having high charge carrier mobilities and conductivities that exceed most other π-conjugated systems. In contrast to most conjugated polymers, the rigid chemical structure of carbon nanotubes prevents polaron formation upon doping,[28] and the porous network morphology of SWCNT bundles appears to be unperturbed by solution-phase doping treatments. These traits simplify the interpretation of charge carrier transport in doped s-SWCNT networks since P3HT solid-state morphology can be dramatically modified by dopant intercalation and the polymer backbone structure plays an important role on the localization and transport properties of the resulting polarons.[25]

For this study, we systematically compare the doping density-dependent transport in high-mobility large-diameter s-SWCNTs that are doped with five unique p-type molecular dopants. These include two small-molecule oxidants, $F_4$TCNQ and triethyloxonium hexachloroantimonate (OA), that we have previously used to tune carrier density in s-SWCNT thin films[9,10,29,30] and three different DDB dopants with distinct electron affinity values. Through calculations of the electrostatic interactions between the injected hole density and the negative counterion, we show that the depth of the coulomb potential wells associated with DDB dopant counterions are reduced with respect to those of smaller counterions. Subsequent analysis of charge

carrier transport in these networks using the SLoT model[18] illustrates that the reduced carrier localization improves charge carrier transport over a wide range of carrier densities.

To connect the observed enhancement in carrier transport to a relevant energy harvesting application for the s-SWCNT thin films, the finely tuned measurements of $\sigma$ and $\alpha$ allow us to calculate a TE power factor (PF = $\alpha^2\sigma$). Consistent with the observation of reduced carrier localization at sterically hindered DDB counterion sites, we find that the plasma torch (PT) s-SWCNT networks doped by these DDB molecules exhibit large TE PFs approaching 1,000 $\mu W\,m^{-1}\,K^{-2}$. This TE performance surpasses that of equivalent networks doped by $F_4TCNQ$ or OA and represents a best in class for enriched s-SWCNT thin-film networks. This proof-of-concept demonstration represents the first application of DDB dopants to any TE material system and highlights the critical role of counterion chemical and electronic structures on the electrical transport of SWCNT materials.

## RESULTS

### Preparation and characterization of enriched s-SWCNT networks

Here, we compare three DDB dopants, perfunctionalized with either 4-(trifluoromethyl) benzyloxy (DDB-$F_{36}$), (2,3,4,5,6-pentafluoro)benzyloxy (DDB-$F_{60}$), or 3,5-bis(trifluoromethyl)benzyloxy (DDB-$F_{72}$) substituents, to the commonly employed p-type dopants $F_4TCNQ$ and OA. The chemical structures of the dopants and their electron affinities (as measured by cyclic voltammetry [CV]) are illustrated in Figure 1A.

The PT synthesis method produces semiconducting and metallic SWCNTs with a distribution of diameters (shown in Figure 1B). The metallic tubes are removed from the distribution using selective extraction of the semiconducting (s-SWCNT) species from the raw nanotube soot via ultrasonication in a solution containing poly[(9,9-di-*n*-dodecyl-2,7-fluorendiyl-dimethine)-(1,4-phenylene-dinitrilomethine)] (PFPD).[10] The remaining s-SWCNTs have a distribution of tube diameters centered around 1.35 nm (see Figure S1) with a corresponding distribution of ionization energies (IEs) centered around 5.15 eV. The reduction potentials and the two-dimensional projected area of the dopant counterions are summarized in Figure 1C. This comparison allows us to explore the impact of both the geometric chemical structure and electronic (redox) properties of the dopant on the doping efficacy and TE transport properties in our enriched PT s-SWCNT networks.

### Charge carrier doping efficacy

Since direct quantitative measurements of charge carrier densities in organic semiconductors have only been demonstrated for a small number of unique systems, we turn to the carrier density-induced bleach of the s-SWCNT optical transitions as a proxy for the injected carrier density.[10,29,31,32] Figures 2A–2C depict the ultraviolet-visible-near-infrared (UV-vis-NIR) absorbance spectra of ~40-nm-thick PT s-SWCNT films doped to various levels with DDB-$F_{72}$, $F_4TCNQ$, and OA. The neutral PT networks display typical absorption bands due to the $S_{11}$, $S_{22}$, and $S_{33}$ excitonic transitions centered at ~0.73, ~1.31, and ~2.7 eV, respectively. For all three dopants, an increase in the dopant density in the PT networks results in an increase in the hole density within the s-SWCNT, pushing the Fermi level away from vacuum and reducing the strength of the $S_{11}$ optical transition due to phase-space filling.[9,33] As hole densities are further increased, electron density is removed from the second van Hove singularity in the valence band, and the $S_{22}$ optical transition begins to bleach. These observations coincide with the onset of a broad free carrier absorbance, the high energy tail of which can be observed below ~0.5 eV. Qualitatively,

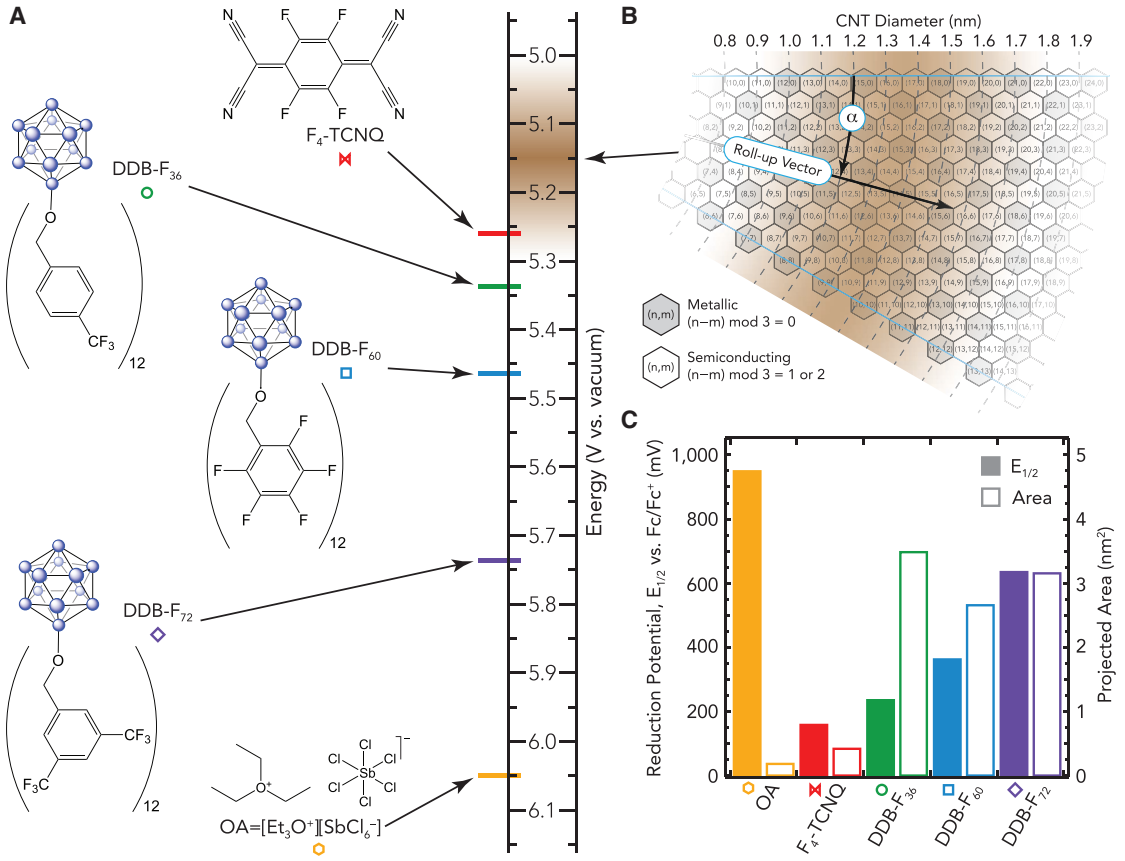


**Figure 1. Chemical and physical properties of the charge-transfer dopants and enriched s-SWCNTs**

(A) Chemical structures of the dopants used in this study and their corresponding electron affinities.

(B) Structure of the enriched PT s-SWCNTS used in this study, with the range of ionization potentials indicated by the brown shaded region in (A).

(C) Measured reduction potentials of the dopants vs. $Fc/Fc^+$ (filled bars) and the two-dimensional area projected by the dopant counterion (empty bars).

similar behavior is observed for samples doped with DDB-$F_{36}$ and DDB-$F_{60}$ (see Figures S2A and S2B).

As in previous studies, we use the fractional absorbance bleach ($\chi = \Delta A/A_0$) as a proxy for the approximate carrier mole fraction (or carrier density relative to a fully doped film), where $A_0$ is the integral of the $S_{11}$ absorption band between 0.55 and 0.85 eV for the neutral (or undoped) network and $\Delta A = A_0 - A_n$ is the change in the integral at a given doping level, $n$.[9,29] The largest bleach magnitude for the $S_{11}$ optical transitions (highest doping levels) in PT s-SWCNT networks was achieved for the OA dopant (cf. Figure 2A), as is consistent for such a potent one-electron oxidant. Although not quite as effective, a significant bleach of the optical transitions was also observed for the network doped with $F_4$TCNQ (cf. Figure 2B). In contrast, a similar magnitude of the bleach of the absorption transitions could not be achieved for samples doped by DDB-$F_{36}$, DDB-$F_{60}$, or DDB-$F_{72}$ (cf. Figures 2C, S2A, and S2B). With regards to the doping efficacy of these p-type dopants, we consider several factors: (1) the reduction potential, or electron affinity, (2) the counterion size, and (3) the solubility.

One attractive feature of the DDB clusters is that the moieties on the benzyloxy functional groups can be chemically tuned to vary the reduction potential (electron

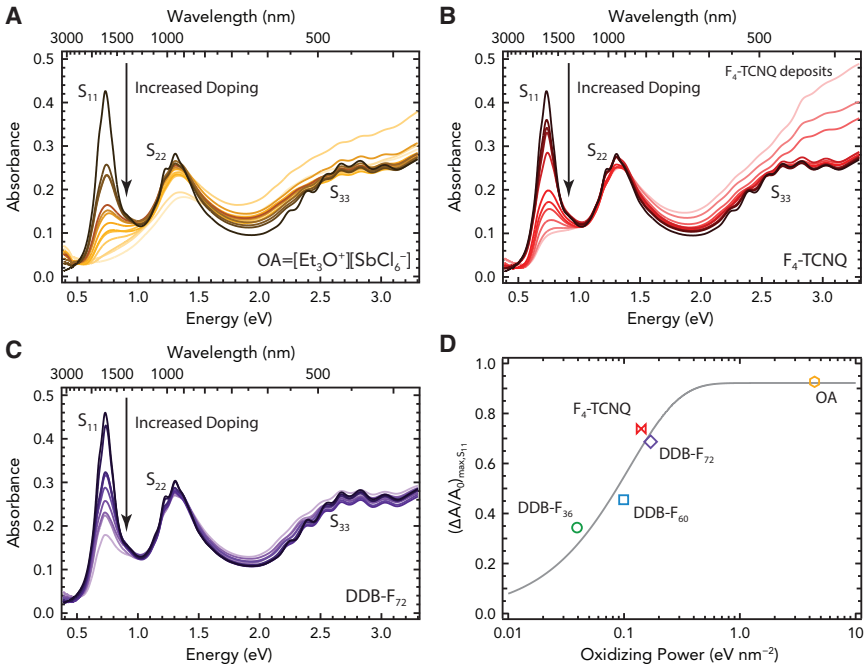


**Figure 2. Tracking charge carrier injection via UV-vis-NIR absorbance**

(A–C) UV-vis-NIR absorbance spectra of PT networks doped with (A) OA, (B) $F_4$TCNQ, and (C) DDB-$F_{72}$.

(D) Maximum fractional absorbance bleach $(\Delta A/A_0)_{max}$ of the integral of the $S_{11}$ excitonic transition envelope, which serves as a proxy for the carrier mole fraction ($\chi$), plotted against the "oxidizing power" of the dopants, which considers both the charge-transfer driving force for doping and the geometrical cross section of the dopant (see text). The gray trend line is a guide for the eye.

affinity).[24–26] For the three DDB dopants employed here, the electron affinity of the clusters increases with the electron-withdrawing nature of the substituents, which, here, correlates with the number of fluorine atoms on the benzyloxy moieties. The reduction potentials, measured using a Ag/AgCl reference electrode and referenced to an internal $Fc/Fc^+$ standard, of DDB-$F_{36}$, DDB-$F_{60}$, and DDB-$F_{72}$ are 237, 364, and 636 mV, respectively (cf. Figure 1C). As would be expected for a doping efficiency that depends on thermodynamic driving force for charge transfer,[34] the maximum $S_{11}$ absorption bleach (carrier density) for PT s-SWCNT networks doped using a 2 mM DDB solution increases with the reduction potential of the DDB dopant (Figure 2D). Consistent with this trend, the OA dopant, which has the largest reduction potential of ~950 mV (estimated via correction of the measured reduction potential[35] using published correction factors for electrochemical measurements employing different standard redox couples[36]) gives rise to the strongest $S_{11}$ absorption bleach.

These observations suggest that the dopant reduction potential (electron affinity) plays an important role in the doping efficacy of the PT s-SWCNT networks, at least for chemically similar dopants. However, the strong bleach of the $S_{11}$ absorption band exhibited for samples doped with a 2 mM solution of $F_4$TCNQ (Figure 2D), despite possessing the smallest reduction potential (~160 mV), points to additional factors that determine the doping efficacy of s-SWCNT networks. We attribute the high doping levels to increased content of $F_4$TCNQ in the network, a factor that could also amplify the efficacy of the OA dopant, as both dopants are much smaller than the DDBs. The increased solubility of $F_4$TCNQ and OA relative to the DDBs could also play a role in the increased doping with these smaller dopants.

Clearly, there are both spatial and geometric factors that limit the accessibility of available carbon nanotube surface areas to the dopant molecules (i.e., doping sites) in the highly porous nanotube network. The three DDB dopant molecules (~2 nm in diameter) employed here are ~2.5 to 4 times larger than $F_4$TCNQ (a planar molecule ~0.5 × ~0.84 nm) and the hexachloroantimonate anion (~0.5 nm in diameter) (Figure 1C). If one considers only the surface area available on the outside of carbon nanotube bundles, this suggests that simple geometric effects (i.e., the packing density of the dopant counterion) likely limit the maximum observable bleach of the optical transitions.

To account for the geometrical cross section of each dopant, we plot the maximum $S_{11}$ bleach vs. a factor that we term the "oxidizing power" of each molecule in Figure 2D. The oxidizing power on the x axis is calculated using a thermodynamic "driving force" for electron transfer (taken here to be the energy difference between the average ionization potential of the PT s-SWCNTs and the electron affinity of the dopant) divided by the two-dimensional projected area of the dopant (i.e., the area the dopant would be expected to take up on a surface). Figure 2D demonstrates that the maximum bleaching magnitude correlates monotonically with this "oxidizing power" and that $F_4$TCNQ is no longer an outlier, suggesting that both the dopant reduction potential and geometrical cross section play a role in the doping efficacy.

We also postulate that $F_4$TCNQ molecules and the hexachloroantimonate anion might be able to infiltrate the carbon nanotube bundles due to their reduced size and to planar geometry in the case of $F_4$TCNQ. This idea is consistent with prior work on the swelling of conjugated polymers, where infiltration of molecules (dopants or fullerenes) depends on the space available in the polymer film due to swelling.[37] Since the SWCNT networks do not swell, the size of the dopant would limit infiltration into the available pores within the relatively tortuous network morphology. The less effective infiltration of the DDB dopants into the solid-state s-SWCNT network is supported by complementary solution-phase doping measurements on isolated s-SWCNTs where DDB-$F_{60}$ doping leads to a larger $S_{11}$ bleach than in the solid-state network (Figure S3). See the supplemental information for further discussion of attempts to improve the doping efficacy of the DDB dopants.

### Doping-dependent carrier transport and (de)localization

To compare the effects of each dopant on charge carrier transport, we measured collinear four-point probe sheet resistance and $\alpha$ for each PT s-SWCNT network as a function of the doping level. Figure 3 depicts $\alpha$ and TE PF ($\alpha^2\sigma$) as a function of $\sigma$ for each PT s-SWCNT network (additional data from Macleod et al.[10] for OA-doped networks is included for comparison with the data collected here). Figure S4 depicts TE transport data as a function of the easy-to-measure fractional absorbance bleach ($\chi = \Delta A/A_0$).

We start our transport analysis at high $\sigma$ using an existing transport model known as the Kang-Snyder model (Equation S1),[17,31] which is derived from the Boltzmann transport equation and relates $\alpha$ and $\sigma$ via a power law transport function. The dependence of $\alpha$ and $\alpha^2\sigma$ on $\sigma$ predicted by the Kang-Snyder model for $s = 1$ and $\sigma_{E0} = 38{,}700$ S m$^{-1}$ (obtained for the OA-doped sample for $\sigma \gtrsim 100{,}000$ S m$^{-1}$) is illustrated by the black traces in Figure 3. A more detailed discussion of the Kang-Snyder model can be found in the supplemental information.

Similar to our previous observations for networks comprised of polymer-wrapped s-SWCNTs produced by the laser vaporization (LV) technique,[31] the polymer-free

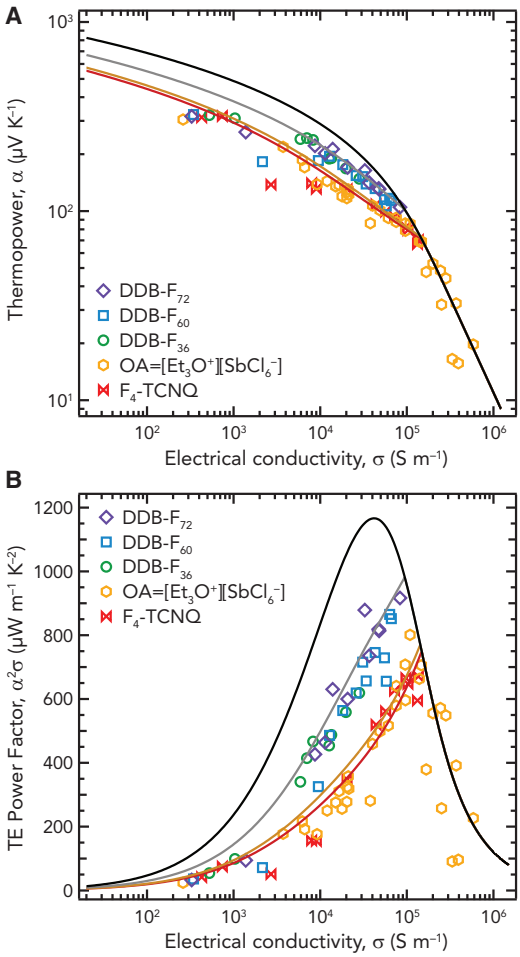


**Figure 3. Doping-dependent thermoelectric properties**

Measured (A) thermopower ($\alpha$) and (B) thermoelectric power factor ($\alpha^2\sigma$) as a function of the electrical conductivity ($\sigma$) for PT networks as a function of doping level for the five different dopants employed in this work. The data for OA-doped networks are a combination of data collected in this study and from MacLeod et al.[10] The Kang-Snyder (black trace) and best-fit SLoT models for the DDB (gray trace), OA (orange trace), and $F_4$TCNQ (red trace) data are plotted.

PT networks exhibit two carrier transport regimes, and the Kang-Snyder model for "intrinsic" phonon-limited transport can only be applied at the higher charge carrier concentrations (in this case, where $\sigma \gtrsim 100{,}000$ S m$^{-1}$). At lower doping levels, the data deviate from the theoretically achievable $\alpha$ predicted by the Kang-Snyder model for $s = 1$. As suggested previously, this indicates the existence of an "extrinsic" transport regime where energetic barriers impose limits on the charge carrier transport. In our previous study of polymer-wrapped LV s-SWCNTs, we tentatively attributed these barriers to inter-nanotube transport (tube-tube or bundle-bundle) junctions related to the network morphology.[31]

More recently, however, the Boltzmann transport equation framework was expanded to an empirically formulated parameterized version of the Kang-Snyder model that includes the effects of transport barriers induced by carrier localization.[18] This semiempirical model, shown in Equation 1, is known as the SLoT model and allows for reproduction of the measured transport data for a number of chemically doped semiconducting polymers and s-SWCNTs.

**Table 1. Semilocalized transport model fit parameters**

| Dopant | $c_{Max}$ (a.u.)[a] | $d$ (nm)[b] | $W_{H,Max}$ (meV) | $W_{H,Slope}$ (meV) |
|---|---|---|---|---|
| $F_4TCNQ$ | 0.8 | 0.35 | 128 | 227 |
| OA | 0.8 | 0.45 | 117 | 210 |
| DDBs | 0.8 | 0.9–1.1 | 72–82 | 150–173 |

Best-fit values to the maximum potential well depth ($W_{H,Max}$) and carrier concentration ratio-dependent slope of the well depth ($W_{H,Slope}$) for the three dopant classes. At high electrical conductivities, the $s = 1$ Kang-Snyder model was best fit using $\sigma_{E0} = 38{,}700$ S m$^{-1}$.

[a]Estimated from the fractional absorbance bleach ($\Delta A/A_0$).

[b]Estimated based on the geometrical structure of the dopant counterions.

$$\sigma_E(E,T,c) = \left\{ \begin{array}{c} 0, (E < E_t) \\ \sigma_0 \exp\left(-\frac{W_H(c)}{k_B T}\right) \times \left(\frac{E - E_t}{k_B T}\right), (E > E_t) \end{array} \right\}, \quad \text{(Equation 1)}$$

where $E_t$ is the energy of the transport edge, $k_B$ is the Boltzmann constant, and $T$ is absolute temperature. The first term in the equation for transport with Fermi level energies above $E_t$ describes hopping-like transport behavior between potential wells separated by $R$ where the well depth, $W_H(c)$, due to charge carrier localization, depends on the carrier concentration ratio, $c$, which is estimated from experimental UV-vis-NIR absorbance and X-ray photoelectron spectroscopy (XPS) data obtained for enriched LV s-SWCNTs (Figures S5).[31] We refer the reader to Gregory et al.[18] for a thorough description of the SLoT model.

In the SLoT model, the potential well depth, width, and separation determine the ability of semilocalized charge carriers to contribute to TE transport. As carrier density increases, the separation between the potential wells, $R$, decreases, causing neighboring wells to overlap and reducing the effective well depth. At a critical doping/carrier density, $R$ becomes sufficiently small such that the carrier density is delocalized and the thermoelectric transport properties reflect those observed within the intrinsic regime. As such, the SLoT model considers both localized and delocalized transport contributions to describe carrier transport more accurately within both the "extrinsic" and "intrinsic" transport regimes, respectively.

Our analyses of the $\alpha$ vs. $\sigma$ data, using estimates of the carrier potential well depths at low carrier densities from linear combination of atomic orbital (LCAO) calculations (*vide infra*) and the SLoT model provided by Gregory et al.,[18] are given by the solid lines in Figures 3A and 3B with the model parameters tabulated in Table 1. We assume an identical $\sigma_{E0}$ for all samples (defined by the high conductivity region of the OA-doped networks) since this should represent the "intrinsic" transport properties of the enriched PT s-SWCNT networks. The model can reproduce the experimentally measured data very well for all three dopant types (we group the data for the DDB-doped networks since there appears to be no clear trend with their reduction potential). When $\sigma < 100{,}000$ S m$^{-1}$, the model indicates a slight increase in $\alpha$ for a given $\sigma$ for the samples doped by any of the three DDB dopants relative to $F_4TCNQ$ and OA. This is consistent with improved carrier transport due to a reduction in the transport barriers, as also emphasized in the TE PF ($\alpha^2\sigma$) vs. $\sigma$ data (Figure 3B), where the peak PF is enhanced and shifts to a lower $\sigma$ value.

Carrier localization has previously been suggested by Eckstein et al. in electrostatically doped monochiral (6,5) s-SWCNT thin films,[19] where the injected carriers were proposed to occupy a potential well with localized charge density that is defined by the electrostatic interaction with a counterion located close to the nanotube sidewall. To

further corroborate and quantify the role of carrier localization in our TE transport measurements, we have extended this previous methodology. We estimate the potential well parameters expected for hole density injected into a PT s-SWCNT that is compensated by the three types of counterions employed here: $F_4$TCNQ, OA, and a functionalized DDB (for the DDB dopants, we ignore the nature of the chemical moiety of the substituents and assume a single size/diameter, taken to be the median of the distribution of diameters for the three different DDB derivatives). We assume that a (16,0) s-SWCNT, with a diameter of ~1.27 nm, is representative of a nanotube from close to the center of the PT diameter distribution and that the carrier-counterion separation, *d*, can be determined for reasonable geometrical configuration(s) of the dopant counterion on the bare s-SWCNT surface. We then use the LCAO method to solve the time-independent Schrödinger equation for a segment of a (16,0) s-SWCNT. We implemented custom code in Igor Pro to obtain the energy eigenstates and wave functions and thus calculate the charge density on the s-SWCNTs. We model the Coulombic interactions of the counterions as point charges and map the injected charge carrier distribution onto the (16,0) segment for three different carrier-counterion separation values (top panels in Figures 4A–4C) corresponding to the three dopant types.

The hole charge carrier distributions along the (16,0) s-SWCNT axis are shown in the bottom panels in Figures 4A–4C and illustrate a decrease in carrier localization with increasing separation between the injected hole and the counterion, as might be expected for a reduction in the electrostatic interaction between the charges. This is further highlighted by the reduction in the binding energy for the injected hole with increasing carrier-counterion separation, *d* (Figure 4D), from ~130 meV for holes bound relatively strongly to the $F_4$TCNQ counterion to ~75 meV for holes bound relatively weakly to the counter-charge localized on the core of a functionalized DDB. This is because the large DDB dopant counteranions have the electron localized on the DDB core at least 1 nm away from the injected hole carrier density on the carbon nanotube, greatly reducing the electrostatic interaction between holes and the counteranions. The net result is enhanced carrier delocalization and improved carrier transport in these enriched s-SWCNT networks.

### Carrier delocalization improves TE performance of s-SWCNT networks

In addition to enabling fundamental insights into carrier delocalization and transport in our doped s-SWCNT networks, tracking both $\sigma$ and $\alpha$ as a function of carrier density allows us to probe the impact of carrier delocalization on the technologically relevant TE PF. Figure 3 demonstrates that the PT s-SWCNT networks doped with DDB-$F_{72}$ reach a peak PF of 917 $\mu W\ m^{-1}\ K^{-2}$, which exceeds the previous best value (PF of ~720 $\mu W\ m^{-1}\ K^{-2}$) for OA-doped or potassium-crown ether (K-CE)-doped PT networks,[10] representing a record PF for enriched s-SWCNT networks. Figure S6, and the associated discussion, provides a comparison of the maximum PF data for enriched s-SWCNT networks presented in the literature. As covered in recent reviews,[3,4] there are other carbon nanotube-based materials with attractive properties for TE energy harvesting, including fibers typically composed of multi-walled carbon nanotubes[38–40] and even enriched metallic SWCNT thin films.[41] Each of these systems, including the s-SWCNT thin films studied here, has its own advantages and disadvantages, but the insights gleaned here for doping-modulated carrier delocalization have the potential to tune and optimize TE performance across this family of materials, as well as other semiconductors where charge carrier densities are modulated using chemical charge-transfer dopants (i.e., conjugated polymers, molecular semiconductors, etc.).

This is the first demonstration of improved TE performance for an organic semiconductor system doped with these sterically hindered DDB dopants and provides a

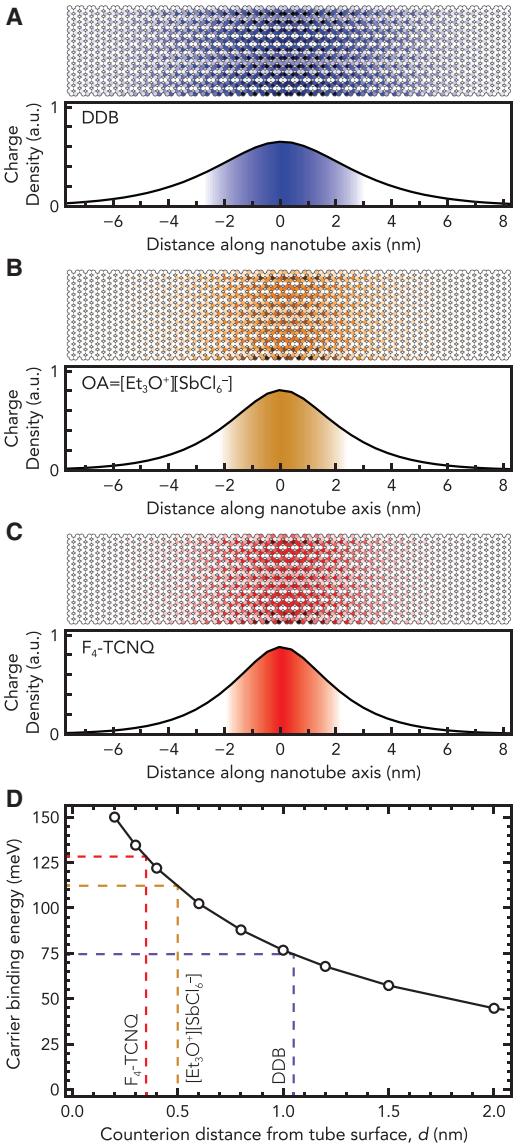


**Figure 4. Charge carrier density distributions and binding energies**

(A–C) Calculated charge carrier density "maps" (top) and distributions (bottom) for a charge injected into a (16,0) s-SWCNT and compensated by a negative counter-charge located either (A) 1.05, (B) 0.5, or (C) 0.35 nm from the nanotube surface, corresponding to doping with a functionalized DDB, OA, and $F_4$TCNQ, respectively.

(D) The calculated binding energy for a carrier localized in a potential well as a function of the carrier-counterion separation, *d*.

proof of concept that the resulting carrier delocalization can improve performance metrics in technologically relevant applications. Broadly speaking, this fundamental strategy could be applied to several other materials and applications. Molecular doping has recently been exploited to improve the performance of bulk heterojunction organic solar cells, organic field-effect transistors, and organic light-emitting diodes. Molecular dopants can also be used to tune carrier density and transport in many nanoscale inorganic semiconductors, such as transition metal dichalcogenide monolayers and semiconductor nanocrystals, both of which hold promise for a variety of opto-electronic applications.

## DISCUSSION

In summary, we have demonstrated that the chemical and geometric structures of redox dopants influence the efficacy of carrier injection into enriched s-SWCNT networks. Although the hole carrier density depends on the reduction potential of functionalized DDB dopants, a larger bleach of the excitonic absorbance bands is observed for smaller dopants (e.g., $F_4$TCNQ and OA). However, calculations suggest that these smaller dopants result in stronger electrostatic interactions between the injected hole density and the negative counterion, localizing the hole onto shorter segments of the s-SWCNTs. This localization results in a larger binding energy for the hole that impedes transport at low charge carrier densities. In contrast, since the extracted electron density is localized on the core of the functionalized DDB dopants, the injected hole density is spatially separated from its countercharge and consequently experiences weaker electrostatic interactions.

The observed dependence of charge transport on the counterion-induced hole localization in enriched s-SWCNT networks can be understood within the context of a SLoT model, offering a clear design rule for the development of a next generation of chemical redox dopants to improve carrier transport in organic semiconductors. Enhanced charge transport in DDB-doped networks enables the demonstration of a peak TE PF ($\sim$920 $\mu W\ m^{-1}\ K^{-2}$) that significantly exceeds the previous best for enriched s-SWCNT networks. Since the doping efficacy of the DDB-based dopants employed here appears to be limited by geometric factors, further studies should focus on improving the doping ability of such dopants and on exploring the impact of these chemical dopants on the transport at higher injected charge carrier densities.

## EXPERIMENTAL PROCEDURES

### Resource availability

#### *Lead contact*

Further information and requests for resources should be directed to and will be fulfilled by the lead contact, Andrew Ferguson (andrew.ferguson@nrel.gov).

#### *Materials availability*

This study did not generate new unique materials.

#### *Data and code availability*

The data presented in this work are available from the corresponding authors upon reasonable request.

### Preparation of enriched plasma torch dispersions and thin-film networks

#### *Starting materials*

Plasma torch power was obtained from NanoIntegris (Batch RNB 776-020-190226). Fullerene contaminants were rinsed from the raw PT SWCNT powder before preparing dispersions. PFPD was synthesized according to literature procedures.[42] The polymer solution was agitated in a heated ultrasonic bath for several minutes to ensure full solvation of the polymer. The neutral species of the redox-active proanions of the type $B_{12}(OCH_2Ar)_{12}$ (Ar = 4-$CF_3C6H_4$ [DDB-$F_{36}$], $C_6F_5$ [DDB-$F_{60}$], 3,5-$(CF_3)_2C_6H_3$ [DDB-$F_{72}$]) were synthesized according to literature procedures.[26] All solvents (toluene, dichloroethane, etc.), trifluoroacetic acid (TFA), $F_4$TCNQ, and OA were obtained from Sigma-Aldrich and used without further purification.

#### *Dispersions*

PT SWCNT powder (16 $\pm$ 0.9 mg) was added to eight canonical vials and mixed with 40 mL anhydrous toluene by vigorous shaking for at least 60 s. The suspensions were

centrifuged with a Fisher Scientific (Marathon 8K) benchtop centrifuge at 4,200 rpm for 20 min. The solvent, containing the fullerene contaminants, was decanted without disturbing the sedimented PT SWCNT solids.

The remaining sediment was mixed with 1.5 mg $mL^{-1}$ PFPD in 15 mL toluene (anhydrous) and transferred to a 20 mL scintillation vial. The nanotube/polymer mixture was then processed in the vial with a probe tip ultrasonic processor (Cole Parmer CPX-750, 1/2″ tip) for 15 min at 40% amplitude (with an indicated output power of ~28 W). To avoid excessive heating of the dispersion during the tip sonication process, the vial was placed in a dry ice/ethanol bath.

Immediately following the ultrasonic process, the contents of the vial were transferred to a centrifuge tube and processed at 13,200 rpm for 5 min at 20°C (Beckman Coulter Optima XE-90 Ultracentrifuge, SW-32 Ti rotor). The supernatant, containing polymer-wrapped s-SWCNTs and excess polymer, was collected via pipette. To minimize the concentration of excess polymer in solution and to capture excess polymer for reuse, this dispersion supernatant was reprocessed but at 24,100 rpm for 20 h at 20°C (Beckman Coulter Optima XE-90 Ultracentrifuge, SW-32 Ti rotor).

The resulting supernatant typically contained only unbound polymer in solution and could be collected for reuse, while the pellet contained polymer-wrapped s-SWCNTs with very little excess polymer. The s-SWCNT ink was then prepared by dispersing the pellet in neat toluene: typically, multiple pellets can be dispersed in one scintillation vial, depending on the desired concentration. The pellet(s):toluene combination was then processed in a heated ultrasonic bath for 5 min or more to yield a homogeneous polymer:s-SWCNT ink.

*Thin-film networks*

Quartz substrates were cleaned with Liquinox/deionized (DI) water solution using an electric toothbrush and then were rinsed with DI water and dried with $N_2$. They were subsequently bath sonicated in acetone for 5 min and then blown dry with $N_2$, and this process was repeated in isopropyl alcohol. The substrates were then placed in a UV-ozone chamber for 5 min.

The ink was then printed at 300 μL $min^{-1}$, directed by a stream of dry nitrogen gas at 7 std.L $min^{-1}$, onto the clean glass substrates on a heated stage (130°C ± 10°C) using an ultrasonic spray head (Sonotek, 0.8 W), with a raster pattern designed to maximize uniformity over the sample area. After printing, the cleavable polymers were removed by submersion in solution of TFA:toluene at 1:100 (by volume) for 10 min at 78°C, followed by submersion in neat toluene for at least 10 min at 78°C. The polymer-removed sample was then dried under nitrogen flow and placed in a vacuum oven at 80°C for 24 hr.

The PT s-SWCNT networks were doped by submersion of the sample in a solution of the chosen dopant in a suitable solvent. Typically, maximal doping occurs when the sample is submerged in solution with a concentration ≥2 mM for at least 1 min at elevated temperatures. To achieve other doping levels and to determine the maximum PF, the doping level can be modified either from the as-printed state by starting at lower dopant concentrations and exposure durations and increasing one or both or by maximally doping the sample initially and sequentially dedoping with increased duration of soaking in a suitable solvent. The solvents used during the treatment of the thin-film networks are denoted, along with their abbreviations, in Table S1 and the full doping history for each sample is located in Tables S2–S6.

### Characterization of the thin-film networks

#### *Four-point colinear sheet resistance*

The sheet resistance of the networks was measured on each sample for all doping levels using a current-voltage (I-V) sweep performed by using a Keithley 2400 Source-Measure Unit (controlled with a laptop running a custom LabView program to perform the measurement and collect experimental data) connected to a Signatone S-302-4 Pro4 Manual Four Point Resistivity Probe station with an SP4-40045OBY probe head. A minimum of 10 measurements were taken on different locations on the film to estimate variability in the electrical transport at each doping level. Sheet resistance values were then converted to conductivity with the film thickness measured by atomic force microscopy (described below).

#### *$\alpha$ Measurements*

$\alpha$ was determined using a custom-built apparatus designed to implement the method of four coefficients, as previously described.[43] The films were situated on top of two closely spaced copper blocks, and thermal and electrical contact between the film and the blocks was established using thin (~2 mm diameter) indium pads on opposite ends of the film. The copper blocks were heated to generate a temperature gradient along the film between the indium pads, and the Seebeck voltage was measured at four different temperature gradients, all near 298 $\pm$ 3 K. $\alpha$ was determined via a linear fit of a plot of Seebeck voltage vs. temperature difference and was corrected for the built-in $\alpha$ associated with the indium pads and copper blocks.

#### *UV-vis-NIR spectroscopy*

All absorbance measurements were performed in ambient conditions on an Agilent Cary 7000 Spectrophotometer, with a step size of 2 nm using a blank substrate to calibrate the baseline before measurement of the sample.

#### *Atomic force microscopy*

Atomic force microscopy (AFM) topography measurements for s-SWCNT film thickness were acquired on a Park AFM equipped with an XE-70 controller operating in intermittent contact mode. For s-SWCNT film thickness measurements, thin scratches were made in the film. Either side of the scratch was imaged using Olympus AC160TS probes with target amplitudes ranging from 0.75 to 1 V. The s-SWCNT film thickness was calculated based on area scans acquired from at least 3 distinct images on independent scratches at different places on the sample. All AFM images were acquired at scan rates ranging from 0.2 to 0.5 Hz at either 512 × 512 or 1,024 × 1,024 resolution.

## SUPPLEMENTAL INFORMATION

Supplemental information can be found online at https://doi.org/10.1016/j.xcrp.2023.101407.

## ACKNOWLEDGMENTS

This work was authored, in part, by the National Renewable Energy Laboratory, operated by the Alliance for Sustainable Energy, LLC, for the US Department of Energy (DOE) under contract no. DE-AC36-08GO28308. The development of the s-SWCNT enrichment process and investigations of charge carrier doping and transport in enriched s-SWCNT networks at NREL were funded by the Solar Photochemistry Program, Division of Chemical Sciences, Geosciences, and Biosciences, Office of Basic Energy Sciences, US DOE. T.L.M. performed the redox doping and TE transport measurements and was supported through an award from the National Science

Foundation INTERN program (NSF Dear Colleague Letter 18–102) provided via NSF award 1934208. Synthetic work on redox-active boron clusters at UCLA, led by A.M.S., was supported as part of the Center for Synthetic Control Across Length-scales for Advancing Rechargeables (SCALAR), an Energy Frontier Research Center funded by the US DOE, Office of Science, Basic Energy Sciences, under award no. DE-SC0019381. Investigations of the redox-active boron cluster doping efficiency of enriched s-SWCNTs networks at UCLA, led by B.J.S., were supported by the National Science Foundation through NSF grant DMR-2105896. K.H.E. and T.H. acknowledge support for the calculations of the charge carrier distribution and binding energies at Julius-Maximilians-Universität Würzburg through the Deutsche Forschungsgemeinschaft grant HE3355/4-1. The views expressed in the article do not necessarily represent the views of the DOE or the US government.

## AUTHOR CONTRIBUTIONS

Conceptualization, T.J.A., A.J.F., and J.L.B.; methodology, T.L.M., T.J.A., A.J.F., and J.L.B.; software, K.H.E. and T.H.; formal analysis, T.L.M.; investigation, T.L.M., T.J.A., and O.L.R.; resources, T.L.M., K.A.T., E.A.D., and J.M.S.; writing – original draft, T.L.M. and A.J.F.; writing – review & editing, T.L.M., T.J.A., O.L.R., A.M.S., B.J.S., T.H., J.L.B., and A.J.F.; visualization, T.L.M., T.H., and A.J.F.; supervision, A.M.S., B.J.S., T.H., J.L.B., and A.J.F.; funding acquisition, J.L.B., T.L.M., A.M.S., and T.H.

## DECLARATION OF INTERESTS

Several of the authors are inventors on US patent nos. 10,598,614 and 10,928,334 and/or US patent application no. 17/150,134, which include claims related to some of the work described herein. UCLA holds patent applications (e.g., US application no. 16/077,415) on several compounds reported in this work from which A.M.S. and current/former co-workers may receive royalty payments. The $B_{12}(OCH_2C_6F_5)_{12}$ cluster (catalog #901272) is commercially available through the MilliporeSigma catalog through a materials transfer agreement between UCLA and MilliporeSigma. T.L.M. is currently affiliated with the Washington Clean Energy Testbeds, operated by the University of Washington Clean Energy Institute.

## INCLUSION AND DIVERSITY

We support inclusive, diverse, and equitable conduct of research. While citing references scientifically relevant for this work, we also actively worked to promote gender balance in our reference list.

Received: November 18, 2022
Revised: March 31, 2023
Accepted: April 13, 2023
Published: May 5, 2023

## REFERENCES

1. Arnold, M.S., Blackburn, J.L., Crochet, J.J., Doorn, S.K., Duque, J.G., Mohite, A., and Telg, H. (2013). Recent developments in the photophysics of single-walled carbon nanotubes for their use as active and passive material elements in thin film photovoltaics. Phys. Chem. Chem. Phys. *15*, 14896–14918. https://doi.org/10.1039/c3cp52752b.

2. Blackburn, J.L. (2017). Semiconducting single-walled carbon nanotubes in solar energy harvesting. ACS Energy Lett. *2*, 1598–1613. https://doi.org/10.1021/acsenergylett.7b00228.

3. Blackburn, J.L., Ferguson, A.J., Cho, C., and Grunlan, J.C. (2018). Carbon-nanotube-based thermoelectric materials and devices. Adv. Mater. *30*, 1704386. https://doi.org/10.1002/adma.201704386.

4. Massetti, M., Jiao, F., Ferguson, A.J., Zhao, D., Wijeratne, K., Würger, A., Blackburn, J.L., Crispin, X., and Fabiano, S. (2021). Unconventional thermoelectric materials for energy harvesting and sensing applications. Chem. Rev. *121*, 12465–12547. https://doi.org/10.1021/acs.chemrev.1c00218.

5. Zorn, N.F., and Zaumseil, J. (2021). Charge transport in semiconducting carbon nanotube networks. Appl. Phys. Rev. *8*, 041318. https://doi.org/10.1063/5.0065730.

6. Lüssem, B., Riede, M., and Leo, K. (2012). Doping of organic semiconductors. Phys. Status Solidi *210*, 9–43. https://doi.org/10.1002/pssa.201228310.

7. Jacobs, I.E., and Moulé, A.J. (2017). Controlling molecular doping in organic semiconductors. Adv. Mater. *29*, 1703063. https://doi.org/10.1002/adma.201703063.

8. Nonoguchi, Y., Ohashi, K., Kanazawa, R., Ashiba, K., Hata, K., Nakagawa, T., Adachi, C., Tanase, T., and Kawai, T. (2013). Systematic conversion of single walled carbon nanotubes into n-type thermoelectric materials by molecular dopants. Sci. Rep. *3*, 3344. https://doi.org/10.1038/srep03344.

9. Avery, A.D., Zhou, B.H., Lee, J., Lee, E.-S., Miller, E.M., Ihly, R., Wesenberg, D., Mistry, K.S., Guillot, S.L., Zink, B.L., et al. (2016). Tailored semiconducting carbon nanotube networks with enhanced thermoelectric properties. Nat. Energy *1*, 16033. https://doi.org/10.1038/nenergy.2016.33.

10. MacLeod, B.A., Stanton, N.J., Gould, I.E., Wesenberg, D., Ihly, R., Owczarczyk, Z.R., Hurst, K.E., Fewox, C.S., Folmar, C.N., Holman Hughes, K., et al. (2017). Large n- and p-type thermoelectric power factors from doped semiconducting single-walled carbon nanotube thin films. Energy Environ. Sci. *10*, 2168–2179. https://doi.org/10.1039/C7EE01130J.

11. Gregg, B.A., Chen, S.-G., and Cormier, R.A. (2004). Coulomb forces and doping in organic semiconductors. Chem. Mater. *16*, 4586–4599. https://doi.org/10.1021/cm049625c.

12. Arkhipov, V.I., Emelianova, E.V., Heremans, P., and Bässler, H. (2005). Analytic model of carrier mobility in doped disordered organic semiconductors. Phys. Rev. B *72*, 235202. https://doi.org/10.1103/PhysRevB.72.235202.

13. Yu, S., Yang, Q., Yu, W., Zhang, J., Liu, J., Jin, S., Guo, X., and Li, C. (2019). Performance enhancement of ternary polymer solar cells induced by tetrafluorotetracyanoquinodimethane doping. Chem. Mater. *31*, 7650–7656. https://doi.org/10.1021/acs.chemmater.9b02520.

14. Chen, Z., Tang, Y., Lin, B., Zhao, H., Li, T., Min, T., Yan, H., and Ma, W. (2020). Probe and control of the tiny amounts of dopants in BHJ film enable higher performance of polymer solar cells. ACS Appl. Mater. Interfaces *12*, 25115–25124. https://doi.org/10.1021/acsami.0c06127.

15. Oyibo, G., Barrett, T., Jois, S., Blackburn, J.L., and Lee, J.U. (2022). All-carbon nanotube solar cell devices mimic photosynthesis. Nano Lett. *22*, 9100–9106. https://doi.org/10.1021/acs.nanolett.2c03544.

16. Zhang, Q., Nam, J.-S., Han, J., Datta, S., Wei, N., Ding, E.-X., Hussain, A., Ahmad, S., Skakalova, V., Khan, A.T., et al. (2022). Large-diameter carbon nanotube transparent conductor overcoming performance–yield tradeoff. Adv. Funct. Mater. *32*, 2103397. https://doi.org/10.1002/adfm.202103397.

17. Dongmin Kang, S., and Jeffrey Snyder, G. (2017). Charge-transport model for conducting polymers. Nat. Mater. *16*, 252–257. https://doi.org/10.1038/nmat4784.

18. Gregory, S.A., Hanus, R., Atassi, A., Rinehart, J.M., Wooding, J.P., Menon, A.K., Losego, M.D., Snyder, G.J., and Yee, S.K. (2021). Quantifying charge carrier localization in chemically doped semiconducting polymers. Nat. Mater. *20*, 1414–1421. https://doi.org/10.1038/s41563-021-01008-0.

19. Eckstein, K.H., Hartleb, H., Achsnich, M.M., Schöppler, F., and Hertel, T. (2017). Localized charges control exciton energetics and energy dissipation in doped carbon nanotubes. ACS Nano *11*, 10401–10408. https://doi.org/10.1021/acsnano.7b05543.

20. Yamashita, Y., Tsurumi, J., Ohno, M., Fujimoto, R., Kumagai, S., Kurosawa, T., Okamoto, T., Takeya, J., and Watanabe, S. (2019). Efficient molecular doping of polymeric semiconductors driven by anion exchange. Nature *572*, 634–638. https://doi.org/10.1038/s41586-019-1504-9.

21. Thomas, E.M., Peterson, K.A., Balzer, A.H., Rawlings, D., Stingelin, N., Segalman, R.A., and Chabinyc, M.L. (2020). Effects of counter-ion size on delocalization of carriers and stability of doped semiconducting polymers. Adv. Electron. Mater. *6*, 2000595. https://doi.org/10.1002/aelm.202000595.

22. Murrey, T.L., Riley, M.A., Gonel, G., Antonio, D.D., Filardi, L., Shevchenko, N., Mascal, M., and Moulé, A.J. (2021). Anion exchange doping: tuning equilibrium to increase doping efficiency in semiconducting polymers. J. Phys. Chem. Lett. *12*, 1284–1289. https://doi.org/10.1021/acs.jpclett.0c03620.

23. Jacobs, I.E., D'Avino, G., Lemaur, V., Lin, Y., Huang, Y., Chen, C., Harrelson, T.F., Wood, W., Spalek, L.J., Mustafa, T., et al. (2022). Structural and dynamic disorder, not ionic trapping, controls charge transport in highly doped conducting polymers. J. Am. Chem. Soc. *144*, 3005–3019. https://doi.org/10.1021/jacs.1c10651.

24. Wixtrom, A.I., Shao, Y., Jung, D., Machan, C.W., Kevork, S.N., Qian, E.A., Axtell, J.C., Khan, S.I., Kubiak, C.P., and Spokoyny, A.M. (2016). Rapid synthesis of redox-active dodecaborane B12(OR)12 clusters under ambient conditions. Inorg. Chem. Front. *3*, 711–717. https://doi.org/10.1039/C5QI00263J.

25. Aubry, T.J., Winchell, K.J., Salamat, C.Z., Basile, V.M., Lindemuth, J.R., Stauber, J.M., Axtell, J.C., Kubena, R.M., Phan, M.D., Bird, M.J., et al. (2020). Tunable dopants with intrinsic counterion separation reveal the effects of electron affinity on dopant intercalation and free carrier production in sequentially doped conjugated polymer films. Adv. Funct. Mater. *30*, 2001800. https://doi.org/10.1002/adfm.202001800.

26. Axtell, J.C., Messina, M.S., Liu, J.Y., Galaktionova, D., Schwan, J., Porter, T.M., Savage, M.D., Wixtrom, A.I., Rheingold, A.L., Kubiak, C.P., et al. (2019). Photooxidative generation of dodecaborate-based weakly coordinating anions. Inorg. Chem. *58*, 10516–10526. https://doi.org/10.1021/acs.inorgchem.9b00935.

27. Aubry, T.J., Axtell, J.C., Basile, V.M., Winchell, K.J., Lindemuth, J.R., Porter, T.M., Liu, J.Y., Alexandrova, A.N., Kubiak, C.P., Tolbert, S.H., et al. (2019). Dodecaborane-based dopants designed to shield anion electrostatics lead to increased carrier mobility in a doped conjugated polymer. Adv. Mater. *31*, 1805647. https://doi.org/10.1002/adma.201805647.

28. Zaumseil, J. (2018). Semiconducting single-walled carbon nanotubes or very rigid conjugated polymers: a comparison. Adv. Electron. Mater. *5*, 1800514. https://doi.org/10.1002/aelm.201800514.

29. Norton-Baker, B., Ihly, R., Gould, I.E., Avery, A.D., Owczarczyk, Z.R., Ferguson, A.J., and Blackburn, J.L. (2016). Polymer-free carbon nanotube thermoelectrics with improved charge carrier transport and power factor. ACS Energy Lett. *1*, 1212–1220. https://doi.org/10.1021/acsenergylett.6b00417.

30. Stanton, N.J., Ihly, R., Norton-Baker, B., Ferguson, A.J., and Blackburn, J.L. (2021). Solution-phase p-type doping of highly enriched semiconducting single-walled carbon nanotubes for thermoelectric thin films. Appl. Phys. Lett. *119*, 023302. https://doi.org/10.1063/5.0055837.

31. Blackburn, J.L., Kang, S.D., Roos, M.J., Norton-Baker, B., Miller, E.M., and Ferguson, A.J. (2019). Intrinsic and extrinsically limited thermoelectric transport within semiconducting single-walled carbon nanotube networks. Adv. Electron. Mater. *5*, 1800910. https://doi.org/10.1002/aelm.201800910.

32. Eckstein, K.H., Oberndorfer, F., Achsnich, M.M., Schöppler, F., and Hertel, T. (2019). Quantifying doping levels in carbon nanotubes by optical spectroscopy. J. Phys. Chem. C *123*, 30001–30006. https://doi.org/10.1021/acs.jpcc.9b08663.

33. Greene, B.I., Orenstein, J., and Schmitt-Rink, S. (1990). All-optical nonlinearities in organics. Science *247*, 679–687. https://doi.org/10.1126/science.247.4943.679.

34. Kunai, Y., Liu, A.T., Cottrill, A.L., Koman, V.B., Liu, P., Kozawa, D., Gong, X., and Strano, M.S. (2017). Observation of the marcus Inverted region of electron transfer from asymmetric chemical doping of pristine (n,m) single-walled carbon nanotubes. J. Am. Chem. Soc. *139*, 15328–15336. https://doi.org/10.1021/jacs.7b04314.

35. Rathore, R., Kumar, A.S., Lindeman, S.V., and Kochi, J.K. (1998). Preparation and structures of crystalline aromatic cation-radical salts. Triethyloxonium hexachloroantimonate as a novel (One-Electron) oxidant. J. Org. Chem. *63*, 5847–5856.

36. Cardona, C.M., Li, W., Kaifer, A.E., Stockdale, D., and Bazan, G.C. (2011). Electrochemical considerations for determining absolute frontier orbital energy levels of conjugated polymers for solar cell applications. Adv. Mater. *23*, 2367–2371. https://doi.org/10.1002/adma.201004554.

37. Aguirre, J.C., Hawks, S.A., Ferreira, A.S., Yee, P., Subramaniyan, S., Jenekhe, S.A., Tolbert, S.H., and Schwartz, B.J. (2015). Sequential processing for organic photovoltaics: design rules for morphology control by tailored semi-orthogonal solvent blends. Adv. Energy Mater.

*5*, 1402020. https://doi.org/10.1002/aenm.201402020.

38. Choi, J., Jung, Y., Yang, S.J., Oh, J.Y., Oh, J., Jo, K., Son, J.G., Moon, S.E., Park, C.R., and Kim, H. (2017). Flexible and robust thermoelectric generators based on all-carbon nanotube yarn without metal electrodes. ACS Nano *11*, 7608–7614. https://doi.org/10.1021/acsnano.7b01771.

39. Sun, T., Zhou, B., Zheng, Q., Wang, L., Jiang, W., and Snyder, G.J. (2020). Stretchable fabric generates electric power from woven thermoelectric fibers. Nat. Commun. *11*, 572. https://doi.org/10.1038/s41467-020-14399-6.

40. Komatsu, N., Ichinose, Y., Dewey, O.S., Taylor, L.W., Trafford, M.A., Yomogida, Y., Wehmeyer, G., Pasquali, M., Yanagi, K., and Kono, J. (2021). Macroscopic weavable fibers of carbon nanotubes with giant thermoelectric power factor. Nat. Commun. *12*, 4931–4938. https://doi.org/10.1038/s41467-021-25208-z.

41. Ichinose, Y., Yoshida, A., Horiuchi, K., Fukuhara, K., Komatsu, N., Gao, W., Yomogida, Y., Matsubara, M., Yamamoto, T., Kono, J., and Yanagi, K. (2019). Solving the thermoelectric trade-off problem with metallic carbon nanotubes. Nano Lett. *19*, 7370–7376. https://doi.org/10.1021/acs.nanolett.9b03022.

42. Lei, T., Chen, X., Pitner, G., Wong, H.S.P., and Bao, Z. (2016). Removable and recyclable conjugated polymers for highly selective and high-yield dispersion and release of low-cost carbon nanotubes. J. Am. Chem. Soc. *138*, 802–805. https://doi.org/10.1021/jacs.5b12797.

43. Young, D.L., Coutts, T.J., Kaydanov, V.I., Gilmore, A.S., and Mulligan, W.P. (2000). Direct measurement of density-of-states effective mass and scattering parameter in transparent conducting oxides using second-order transport phenomena. J. Vac. Sci. Technol. A *18*, 2978–2985. https://doi.org/10.1116/1.1290372.